Open access • Journal Article • DOI:10.1007/S11012-013-9862-0

Phase-field models for brittle and cohesive fracture — Source link

Julien Vignollet, Stefan May, René de Borst, Clemens V. Verhoosel

Institutions: University of Glasgow, Eindhoven University of Technology

Published on: 21 Jan 2014 - Meccanica (Springer Netherlands)

Topics: Cohesive zone model, Fracture mechanics, Brittleness, Fracture (geology) and Phase field models

---

Article:
Vignollet, J., May, S., de Borst, R. orcid.org/0000-0002-3457-3574 et al. (1 more author) (2014) Phase-field models for brittle and cohesive fracture. Meccanica, 49 (11). pp. 2587-2601. ISSN 0025-6455

https://doi.org/10.1007/s11012-013-9862-0

Noname manuscript No.
(will be inserted by the editor)

Phase-field models for brittle and cohesive fracture

Julien Vignollet · Stefan May · René de Borst · Clemens V. Verhoosel

Received: date / Accepted: date

Abstract In this paper we first recapitulate some basic notions of brittle and cohesive fracture models, as well as the phase-field approximation to fracture. Next, a critical assessment is made of the sensitivity of the phase-field approach to brittle fracture, in particular the degradation function, and the use of monolithic *vs* partitioned solution schemes. The last part of the paper makes extensions to a recently developed phase-field model for cohesive fracture, in particular for propagating cracks. Using some simple examples the current state of the cohesive phase-field model is shown.

Keywords Phase-field models · brittle fracture · cohesive fracture · damage

1 Introduction

The modelling of discontinuities, including interfaces, is of a growing importance in the mechanics of materials. Basically, two methods exist to capture discontinuities: one can either distribute them over a finite width, or handle them as true discontinuities, i.e. in a discrete sense.

Julien Vignollet
School of Engineering, University of Glasgow
E-mail: Julien.Vignollet@glasgow.ac.uk

Stefan May
School of Engineering, University of Glasgow
E-mail: S.May.2@research.gla.ac.uk

René de Borst
School of Engineering, University of Glasgow
E-mail: Rene.DeBorst@glasgow.ac.uk

Clemens V. Verhoosel
Department of Mechanical Engineering
Eindhoven University of Technology
E-mail: C.V.Verhoosel@tue.nl

When a discontinuity has a stationary character, such as in grain boundaries, it is fairly straightforward to describe it in a discrete manner, since it is then possible to create a conforming mesh such that the discontinuity, either in displacements or in displacement gradients, is modelled explicitly. An evolving or moving discontinuity is more difficult to capture. A possibility is to adapt the mesh upon every change in the topology, as was done by Ingraffea and co-workers in the context of linear elastic fracture mechanics [16], and later for cohesive fracture [9].

Another approach is to model fracture within the framework of continuum mechanics. A fundamental problem then emerges, namely that standard continuum models do not furnish a *non-zero length scale* which is indispensable for describing fracture. To remedy this deficiency, regularisation methods have been proposed, including nonlocal averaging, the addition of viscosity or rate dependency, or the inclusion of couple stresses or higher-order strain gradients [5]. The effect of these strategies is that the discontinuity is transformed into a continuous displacement distribution. The internal length scale is set by the constitutive model, and for a sufficiently fine discretisation, the numerically calculated results are objective with respect to mesh refinement. Particularly in damage mechanics, gradient approaches have gained popularity [20].

Not unrelated to gradient damage approaches are the phase-field models for fracture. However, the point of departure is completely different. In gradient damage models an intrinsically mechanical approach is adopted, and the damage model is regularised by adding gradients to restore well-posedness of the boundary value problem in the post-peak regime. The basic idea in phase-field models, on the other hand, is to replace the zero-width discontinuity by a small, but finite zone with

sharp gradients in a mathematically consistent manner. Indeed, the latter requirement inevitably leads to spatial derivatives in the energy functional, similar to gradient damage models. The first attempts to apply phase-field models for fracture have focused on brittle fracture. Pioneering work has been done in References [6,7,12], where a phase-field approximation was proposed for the variational approach to brittle fracture. Subsequently, a phase-field formulation for brittle fracture was derived based on thermodynamical considerations [18,19]. Applications to dynamic brittle fracture can be found in References [4,8,15].

An extension of the variational formulation for brittle fracture to cohesive fracture has been considered in [7], and a phase-field approximation has been developed in [22], with a focus on the application to adhesive fracture, i.e. debonding along a predefined interface. As pointed out in Reference [22] models for brittle and cohesive fracture rely on very different concepts, and the development of a cohesive phase-field model is a non-trivial task.

In this contribution we will first review some basic concepts in brittle and cohesive fracture, and in phase-field modelling. Next, we will assess the performance of recently proposed brittle phase-field models at the hand of an established example and an elementary one-dimensional bar, where we investigate a number of factors that can critically affect the performance of phase-field models in brittle fracture. A contribution on how to apply phase-field models to propagating cohesive cracks follows in Section 4, accompanied by revisiting the one-dimensional example analysed before using a brittle phase-field model, and a two-dimensional example also analysed in [22].

2 Fracture and phase-field models

2.1 Brittle and cohesive fracture

We consider a volume Ω with an internal discontinuity boundary Γ_d as shown in Figure 1. As a starting point we consider the potential energy for the case of a discrete description of brittle fracture in the Griffith sense [12]:

$$\Psi_{\text{pot}} = \int_{\Omega} \psi^e(\boldsymbol{\varepsilon})\,\mathrm{d}V + \int_{\Gamma_d} \mathcal{G}_c\,\mathrm{d}A \tag{1}$$

with the elastic energy density ψ^e a function of the infinitesimal strain tensor $\boldsymbol{\varepsilon}$. The elastic energy density is expressed by Hooke's law for an isotropic linear elastic material as $\psi^e(\boldsymbol{\varepsilon}) = \frac{1}{2}\lambda\varepsilon_{ii}\varepsilon_{jj} + \mu\varepsilon_{ij}\varepsilon_{ij}$ with λ and μ the Lamé constants, and the summation convention applies. In Equation (1) the fracture energy, i.e. the amount of energy dissipated upon the creation of a unit of fracture surface is denoted by $\mathcal{G}_c$. The potential energy Ψ_{pot} governs the balance between elastic energy in the bulk material and the fracture energy.

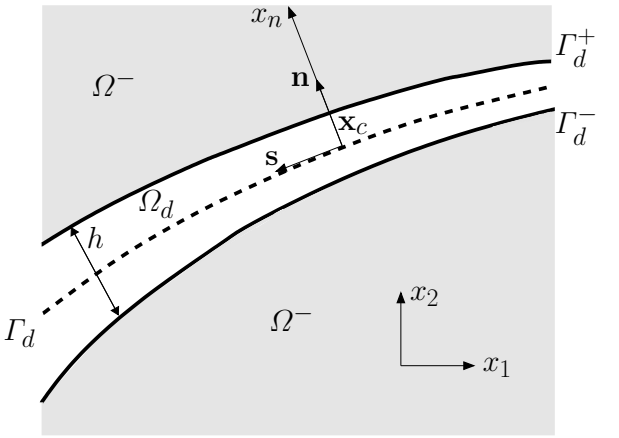

Fig. 1: Cohesive surfaces at an internal discontinuity Γ_d

Most engineering materials are not perfectly brittle in the Griffith sense, but display some ductility after reaching the strength limit. In most cases, there exists a zone ahead of the crack tip, in which small-scale yielding, micro-cracking and void initiation, growth and coalescence take place. If this fracture process zone is sufficiently small compared to the structural dimensions, brittle fracture models can be used, but otherwise the cohesive forces that exist in this fracture process zone must be taken into account. The most powerful and natural way is to use cohesive surface models, which were introduced in [2,11].

An essential difference between brittle and cohesive fracture models is the dependence of the fracture energy on the crack opening. The fracture energy is released only gradually, and energy dissipation is governed by a *fracture energy function*:

$$\mathcal{G} = \mathcal{G}(\llbracket \boldsymbol{u} \rrbracket, \kappa), \tag{2}$$

which depends on the jump of the displacement field $\llbracket \boldsymbol{u} \rrbracket$ across the discontinuity Γ_d and on a history parameter κ, which obeys the Kuhn-Tucker loading/unloading conditions. The potential energy now takes the form:

$$\Psi_{\text{pot}} = \int_{\Omega} \psi^e(\boldsymbol{\varepsilon})\mathrm{d}V + \int_{\Gamma_d} \mathcal{G}(\llbracket \mathbf{u} \rrbracket, \kappa)\mathrm{d}A \tag{3}$$

and the cohesive tractions $\boldsymbol{t}_d$ are obtained through differentiation of the fracture energy function with respect to the crack opening:

$$\boldsymbol{t}_d = \frac{\partial \mathcal{G}}{\partial \llbracket \boldsymbol{u} \rrbracket} \quad \rightarrow \quad \boldsymbol{t}_d = \boldsymbol{t}_d(\llbracket \boldsymbol{u} \rrbracket, \kappa). \tag{4}$$

2.2 Phase field approximations

As the starting point of the derivation of the phase field approximation to fracture, we use the Dirac function δ to relate the infinitesimal surface area $\mathrm{d}A$ at $\mathbf{x}_c \in \Gamma_d$ to the infinitesimal volume $\mathrm{d}V$ of the surrounding body:

$$\mathrm{d}A(\mathbf{x}_c) = \int_{-\infty}^{\infty} \delta\left(x_n\right)\, \mathrm{d}V, \tag{5}$$

where x_n is a coordinate in the direction normal to the crack, Figure 1. Equation (5) allows for smeared descriptions of the fracture surface by an approximation of the Dirac function. As in Reference [4] we consider the approximated Dirac function

$$\delta_\ell(x_n) = \frac{1}{2\ell}\exp\left(-\frac{|x_n|}{\ell}\right) \tag{6}$$

with $\ell > 0$ a length scale parameter. Evidently

$$\int_{-\infty}^{\infty} \delta_\ell(x_n)\mathrm{d}x_n = 1 \tag{7}$$

for arbitrary ℓ. The corresponding infinitesimal fracture surface area then follows from

$$\mathrm{d}A_\ell(\mathbf{x}_c) = \int_{-\infty}^{\infty} \delta_\ell\left(x_n\right)\, \mathrm{d}V. \tag{8}$$

A fundamental problem with the smeared Dirac function approximation, Equation (6), is that it is not straightforward to generalise it to more dimensions. Therefore, rather than using this approximate function directly, it is obtained implicitly through the solution of the boundary value problem

$$\begin{cases} d - 4\ell^2 \frac{\mathrm{d}^2 d}{\mathrm{d}x_n^2} = 0 & x_n \in \mathbb{R}\backslash 0 \\ d = 1 & x_n = 0 \\ d = 0 & x_n = \pm\infty \end{cases} \tag{9}$$

with $d(x_n) \in [0,1]$ a scalar field, which equals 1 at the centre of the discontinuity, i.e. for $x_n = 0$, and vanishes for $x_n = \pm\infty$. When $d(0) = 1$ is not imposed, solution of the differential equation (9) is equivalent to minimising

$$I(d) = \frac{1}{4}\int_\Omega \left(d^2 + 4\ell^2 \frac{\mathrm{d}d}{\mathrm{d}x_n}\right)\mathrm{d}V. \tag{10}$$

Since $\mathrm{d}V = \Gamma \mathrm{d}x_n$, we have

$$I(e^{-|x_n|/\ell}) = \ell\Gamma \tag{11}$$

where the crack surface can be expressed through the following volume integral:

$$\Gamma = \int_\Omega \gamma_\ell \mathrm{d}V \tag{12}$$

with the crack density

$$\gamma_\ell = \left(\frac{1}{4\ell}d^2 + \ell\|\nabla d\|^2\right), \tag{13}$$

which is the multi-dimensional generalisation of $\delta_\ell(x_n)$.

3 Brittle fracture

3.1 Derivation

We will now briefly review phase-field models developed for brittle fracture. These models originate from the work of Francfort, Bourdin and Marigo [6,7,12], and have been revisited and improved recently in [1,17,18].

There is a two-way coupling between the regularised crack topology introduced in Section 2 and the mechanical field. In a first step, the a priori unknown crack surface is approximated by the crack density function γ_ℓ, cf. Equations (12) - (13). This allows us to express the work required to create a unit crack area as a volume integral which depends on the phase field variable d and the fracture energy $\mathcal{G}_c$:

$$\int_{\Gamma_d} \mathcal{G}_c \mathrm{d}A = \int_\Omega \mathcal{G}_c \gamma_\ell(d, \nabla d)\, \mathrm{d}V. \tag{14}$$

The other step is inspired by concepts developed in damage mechanics and relies on the assumption that the evolution of the phase field is directly related to crack growth. As such it can be used to model the loss of stiffness of the bulk of the solid. This is achieved by the introduction of a degradation function $g = g(d)$, which must satisfy the following properties:

$$\begin{cases} g : [0,1] \to [0,1] \\ g'(d) < 0 \quad d \in [0,1[\\ g'(1) = 0 \end{cases} \tag{15}$$

These properties are mathematically and physically motivated, and are required to ensure damage propagation and to provide an upper bound to the phase field d variable of 1 [18]. But the actual choice of this function has no physical relevance. A quadratic polynomial is the most widely used one:

$$g(d) = (1-d)^2. \tag{16}$$

More recently, Borden [3] introduced a cubic degradation function:

$$g_s(d) = s((1-d)^3 - (1-d)^2) + 3(1-d)^2 - 2(1-d)^3. \tag{17}$$

As will be discussed in Section 3.3, the main advantage over the quadratic function is that it prevents the emergence of spurious damage away from the crack tip. It also better mimics a linear elastic-brittle behaviour. This is due to the fact that $\lim_{s\to 0} g_s'(0) = 0$, which prevents damage initiation from the initial increase in the phase field. However, Γ-convergence has so far only been proved for the quadratic degradation function [10].

In [6] the degradation function g was multiplied with the elastic energy density of the undamaged state, ψ_0,

such that the elastic energy density of the damaged state reads:

$$\psi^e(\boldsymbol{\varepsilon}, d) = g(d)\psi_0(\boldsymbol{\varepsilon}). \tag{18}$$

This formulation was subsequently refined to account for the fact that damage evolution occurs under different straining modes [1,4,13,17], and it was assumed that the elastic energy of the undamaged state can be additively decomposed into a damaged and an intact part, $\psi_0 = \psi_0^{\mathrm{d}} + \psi_0^{\mathrm{i}}$, so that the degradation function g only acts on the damaged part:

$$\psi^e(\boldsymbol{\varepsilon}, d) = g(d)\psi_0^{\mathrm{d}}(\boldsymbol{\varepsilon}) + \psi_0^{\mathrm{i}}(\boldsymbol{\varepsilon}). \tag{19}$$

This split can result from the decomposition of the strain tensor into positive and negative strain components, or from that into spherical and deviatoric strain components. Substituting Equations (14) and (19) into Equation (1) yields the smeared form of the total potential energy for brittle fracture:

$$\Psi = \int_\Omega g(d)\psi_0^{\mathrm{d}}(\boldsymbol{\varepsilon}) + \psi_0^{\mathrm{i}}(\boldsymbol{\varepsilon}) + \mathcal{G}_c\gamma_l(d, \nabla d)\, \mathrm{d}V. \tag{20}$$

Minimisation of Ψ and introduction of the history field $\mathcal{H}$ to enforce irreversibility [18] lead to the strong form:

$$\operatorname{div}\boldsymbol{\sigma}(\boldsymbol{\varepsilon}, d) = \mathbf{0} \qquad \mathbf{x} \in \Omega \tag{21a}$$

$$\boldsymbol{\sigma}\mathbf{n} = \bar{\mathbf{t}} \qquad \mathbf{x} \in \Gamma_t \tag{21b}$$

$$\mathbf{u} = \bar{\mathbf{u}} \qquad \mathbf{x} \in \Gamma_u \tag{21c}$$

$$\mathcal{G}_c\Big(\frac{d}{2\ell^2} - 2\Delta d\Big) = \frac{\partial g}{\partial d}\mathcal{H} \qquad \mathbf{x} \in \Omega \tag{21d}$$

$$\nabla d \cdot \mathbf{n} = 0 \qquad \mathbf{x} \in \Gamma \tag{21e}$$

where $\bar{\mathbf{t}}$ and $\bar{\mathbf{u}}$ are the prescribed boundary tractions and displacements, respectively, with $\Gamma_t \cup \Gamma_u = \Gamma$ and $\Gamma_t \cap \Gamma_u = \emptyset$. The Cauchy stress $\boldsymbol{\sigma}$ and history field $\mathcal{H}$ read:

$$\boldsymbol{\sigma}(\boldsymbol{\varepsilon}, d) = g(d)\frac{\partial \psi_0^{\mathrm{d}}}{\partial \boldsymbol{\varepsilon}} + \frac{\partial \psi_0^{\mathrm{i}}}{\partial \boldsymbol{\varepsilon}} \tag{22}$$

$$\mathcal{H}(t) = \max_t \psi_0^{\mathrm{d}}(t). \tag{23}$$

The weak form of Equation (21) can be derived in a standard fashion. The finite element approximation of the domain problem involves the following approximations of the field variables and their derivatives:

$$\begin{cases} \mathbf{u}(\mathbf{x}) = \mathbf{N}_u(\mathbf{x})\mathbf{u}^e \\ d(\mathbf{x}) = \mathbf{N}_d(\mathbf{x})\mathbf{d}^e \end{cases} \qquad \begin{cases} \boldsymbol{\varepsilon}(\mathbf{x}) = \mathbf{B}_u(\mathbf{x})\mathbf{u}^e \\ \dfrac{\partial d(\mathbf{x})}{\partial \mathbf{x}} = \mathbf{B}_d(\mathbf{x})\mathbf{d}^e \end{cases} \tag{24}$$

In order to capture possible snapback behaviour, the finite element formulation was augmented by a dissipation-based arc-length solver [14,21]. The resulting set of coupled, nonlinear equations is linearised and solved using a Newton-Raphson iterative scheme, which gives the iterative change of the state vector at iteration k:

$$\begin{bmatrix} \delta\mathbf{d} \\ \delta\mathbf{u} \\ \delta\lambda \end{bmatrix}_k = \begin{bmatrix} \mathbf{K}_{dd} & \mathbf{K}_{du} & \mathbf{0} \\ \mathbf{K}_{ud} & \mathbf{K}_{uu} & -\hat{\mathbf{f}}^{\mathrm{ext}} \\ \mathbf{0}^T & \mathbf{h}^T & w \end{bmatrix}_{k-1}^{-1} \begin{bmatrix} -\mathbf{f}_d^{\mathrm{int}} \\ \lambda\hat{\mathbf{f}}^{\mathrm{ext}} - \mathbf{f}_u^{\mathrm{int}} \\ -\psi \end{bmatrix}_{k-1} \tag{25}$$

with

$$\mathbf{f}_d^{\mathrm{int}} = \int_\Omega \left[\mathcal{G}_c\left(\frac{1}{2l}\mathbf{N}_d^{\mathrm{T}}\mathbf{N}_d + 2l\mathbf{B}_d^{\mathrm{T}}\mathbf{B}_d\right)\mathbf{d} + \frac{\partial g}{\partial d}\mathcal{H}\mathbf{N}_d^{\mathrm{T}}\right] \mathrm{d}V \tag{26}$$

$$\mathbf{f}_u^{\mathrm{int}} = \int_\Omega \mathbf{B}_u^{\mathrm{T}}\left(g\mathbf{D}^{\mathrm{d}} + \mathbf{D}^{\mathrm{i}}\right)\mathbf{B}_u\mathbf{u}\mathrm{d}V \tag{27}$$

$$\psi = \frac{1}{2}\hat{\mathbf{f}}^{\mathrm{ext}}\left(\lambda_0\Delta\mathbf{u} - \Delta\lambda\mathbf{u}_0\right) - \Delta\tau \tag{28}$$

$$\mathbf{K}_{dd} = \frac{\partial \mathbf{f}_d^{\mathrm{int}}}{\partial \mathbf{d}} \quad \mathbf{K}_{du} = \frac{\partial \mathbf{f}_d^{\mathrm{int}}}{\partial \mathbf{u}} \tag{29}$$

$$\mathbf{K}_{ud} = \frac{\partial \mathbf{f}_u^{\mathrm{int}}}{\partial \mathbf{d}} \quad \mathbf{K}_{uu} = \frac{\partial \mathbf{f}_u^{\mathrm{int}}}{\partial \mathbf{u}} \tag{30}$$

$$\mathbf{h} = \frac{\partial \psi}{\partial \mathbf{u}} \quad w = \frac{\partial \psi}{\partial \lambda} \tag{31}$$

where $\hat{\mathbf{f}}^{\mathrm{ext}}$ is the normalised load vector, λ is the load factor, $\Delta\tau$ is the incremental dissipation, and $\mathbf{D}^{\mathrm{d}}$ and $\mathbf{D}^{\mathrm{i}}$ correspond to the damaged and intact parts of the elasticity matrix, respectively. λ_0 and $\mathbf{u}_0$ are the converged values for the load factor and displacements of the previous increment.

3.2 Example 1: Single edge notched plate in pure shear

In order to verify the implementation of the brittle model, a notched square plate of unit length, Figure 2, is subjected to a shear loading. This benchmark test has been examined for instance in [3,18]. The material parameters are $\lambda = 121.15$MPa, $\mu = 80.77$MPa and $\mathcal{G}_c = 2.7 \cdot 10^{-3}$N/mm. The bottom edge is fixed, and the top edge is moved horizontally by $\bar{u}$. The vertical displacements are prevented on the entire boundary Γ, including on the initial notch. Following [18], the strain tensor was decomposed into positive and negative components, and irreversibility was enforced by using the history field $\mathcal{H}$.

The results are shown in Figure 3, and were obtained using a monolithic scheme, a 100x100-element mesh of linear quadrilaterals, and a length scale $\ell = 0.02$mm. The results are in good agreeement with those in [18]. This example shows the qualitative capabilities of the brittle phase field formulation: the model is able

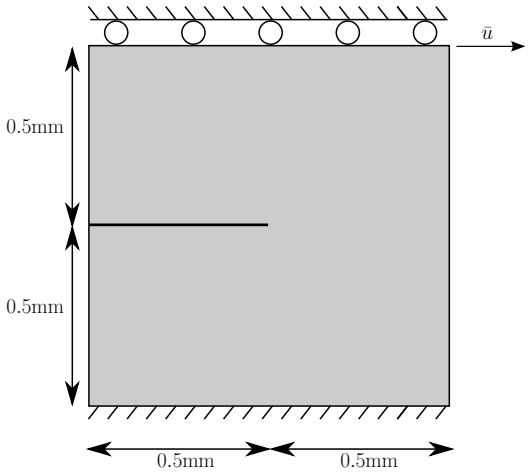

Fig. 2: Notched plate: the top edge is moved horizontally by $\bar{u}$

to track the evolution of cracks of arbitrary geometries and to predict the nonlinear force-displacement relationship until complete failure.

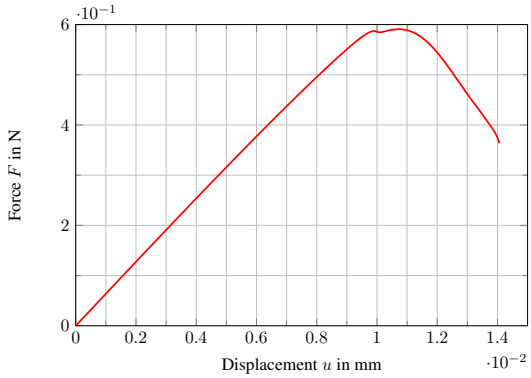

(a) Force-displacement

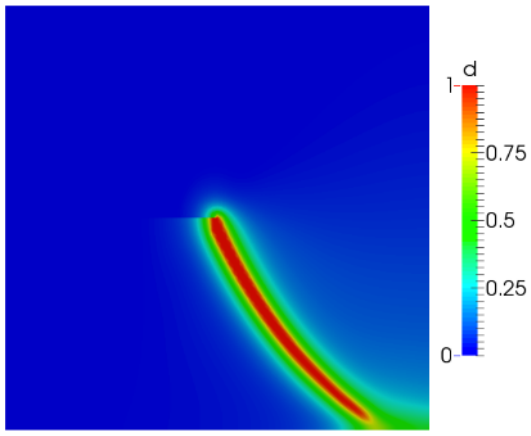

(b) Phase field contour plot

Fig. 3: Response of the notched plate under shear loading

3.3 Example 3: Bar with reduced stiffness in the middle under tension

Next, the one-dimensional bar of Figure 4 is considered. The bar has a reduced thickness in the centre and is loaded at the right edge by a force $\lambda \hat{f}$. The Young's modulus is $E = 10\text{MPa}$ and the fracture toughness $\mathcal{G}_c = 0.1\text{N/mm}$. The bar has a length $L = 1\text{mm}$ and a thickness $b = 1\text{mm}$. The length scale parameter is chosen to be $\ell = \frac{L}{20}$. Since the problem is one-dimensional, $\psi_0^{\mathrm{d}} = E$ and $\psi_0^{\mathrm{i}} = 0$, so that the degradation function g directly acts on the Young's modulus E.

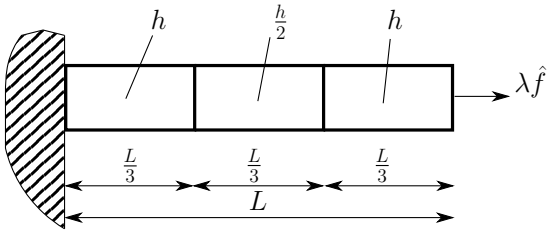

Fig. 4: 1D tension test for a bar with a reduced thickness in the centre

Inspection of the strong form, Equation (21d), shows that at the onset of loading the 'driving force' term $g'\mathcal{H} = g'\psi_0^{\mathrm{d}}(\varepsilon)$ starts to grow, forcing the phase field, and consequently also the crack density γ_ℓ, to increase along the entire bar. As shown by Equation (14), this process dissipates energy, which explains the early departure from linearity of the force-displacement curve in Figure 5.

Next, the importance of using a monolithic solver for this nonlinear problem is studied. For a constant mesh size (150 elements, $h = 0.0067\text{mm}$) and a length scale $\ell = 0.05\text{mm}$, the response of the system for the staggered and the monolithic schemes is compared. Figure 6 shows that the staggered scheme is very sensitive to the size of the load increments, and has not converged for the smallest step size. Indeed, the gain in expended effort per load step for the staggered scheme is easily compensated by the smaller number of steps needed in the monolithic scheme to achieve the same accuracy.

The dependence on the length scale ℓ is shown in Figure 7 for a constant mesh size (150 elements, $h = 0.0067\text{mm}$), which respects the rule of thumb $\ell > h$ to accurately approximate the crack topology as proposed in [19]. Clearly, an increasing length scale results in a decreasing peak force. This makes it difficult to interpret the length scale parameter for the brittle model.

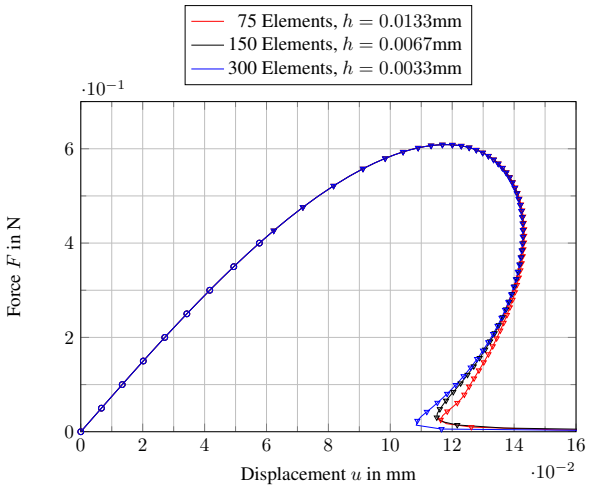

Fig. 5: Mesh refinement study for a constant length scale $\ell = 0.05$mm. The circles denote loading steps where force control has been used and the triangles denote the steps where arc-length control has been used

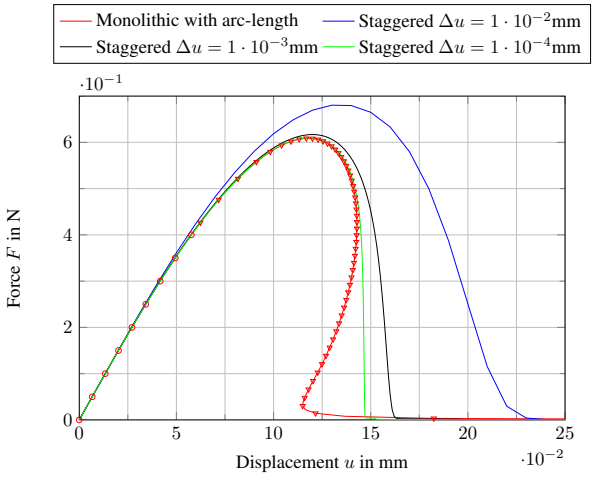

Fig. 6: Comparison of the monolithic and the staggered approaches for $\ell = 0.05$mm with a constant mesh size (150 elements, $h = 0.0067$mm)

On one hand, ℓ has been introduced on purely mathematical ground, Section 2, which is independent from the mechanical field problem. On the other hand, when linking the phase field and the mechanical field, the length scale parameter seems to behave like a material parameter, cf. [1,4].

From Figures 5 - 7 it appears that the brittle model does not exhibit linear elastic behaviour prior to softening. Instead, the curves show nonlinearity from the very beginning. Therefore, a cubic degradation function has been proposed in [3], which results in a linear behaviour up to the peak force. The drawback of this function is that an additional parameter s is introduced,

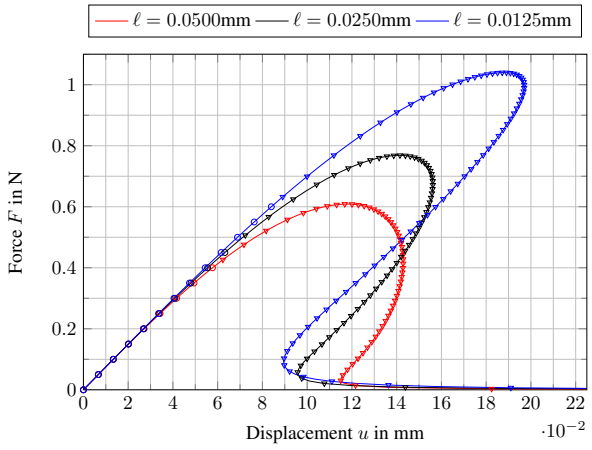

Fig. 7: Influence of the length scale parameter ℓ for a constant mesh size (150 elements, $h = 0.0067$mm)

cf. Equation (17). The quadratic and the cubic degradation functions are compared in Figure 8 using different parameters s. For $s \to 0$ the peak force converges to a unique value [3].

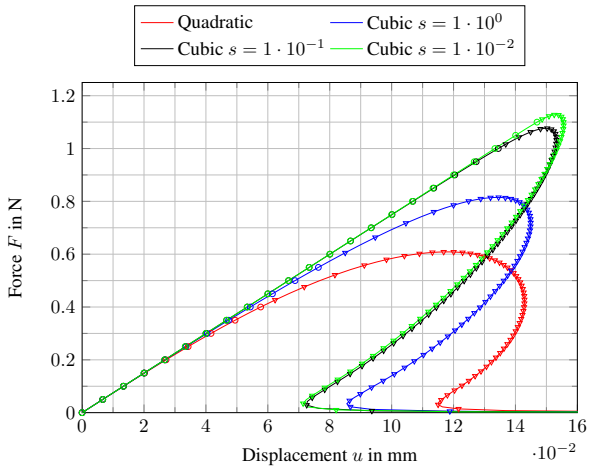

Fig. 8: Comparison of the quadratic and cubic degradation functions

Finally, the approximated crack length Γ_ℓ is examined using Equation (12). The relative error is given by

$$\Gamma_{\mathrm{E}} = \frac{\Gamma_\ell - \Gamma}{\Gamma}, \tag{32}$$

where the exact crack length is $\Gamma_d = h/2 = 0.5$mm. As Figure 9 shows, this is a rather crude approximation due to the fact that the model predicts a damaged zone which spans the entire weakened part of the bar. The tendency that is displayed by the circles *vs* the triangles in Figure 9 suggests that this can be improved by

reducing the length of the bar in the centre. However, there is a concern that upon a reduction of the length scale, the approximation for the crack length deteriorates (although $\ell \gg h$).

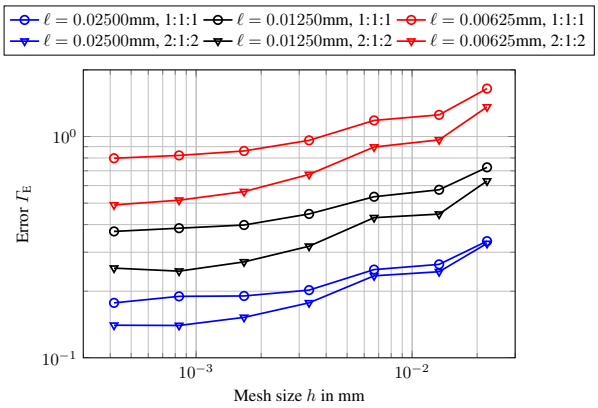

Fig. 9: Error I_E for the final approximated crack length I_l. The circles denote a bar with a ratio 1:1:1, the triangles denote a bar with a ratio 2:1:2

4 Cohesive fracture

The objective of this section is to revisit the phase-field model for cohesive fracture proposed in Reference [22] and to show some further developments that allow for the modelling of propagating cracks. Firstly, the main features of the model are summarised. Refinements and modifications are presented next, followed by some examples.

4.1 The mechanical field problem

Similar to the brittle model, the coupling between the phase field and the mechanical field problems requires the introduction of phase-field quantities in the potential in order to smear out the crack surface.

Like the brittle model presented in Section 3, the topology of the smeared crack is introduced in the expression of the energy dissipation $\mathcal{D}$, and the second term of Equation (3) is rewritten as:

$$\mathcal{D} = \int_{\Gamma} \mathcal{G}(\llbracket \mathbf{u} \rrbracket, \kappa) \mathrm{d}A = \int_{\Omega} \mathcal{G}(\llbracket \mathbf{u} \rrbracket, \kappa) \gamma_\ell(d, \nabla d) \mathrm{d}V \qquad (33)$$

with $\mathcal{G}(\llbracket \mathbf{u} \rrbracket, \kappa)$ the fracture energy function. Equation (33) transforms a discrete crack into a crack that is smeared over a finite length orthogonal to the crack surface, see also Figure 10. Formally, the smeared cohesive zone is defined by $d(\mathbf{x}) > 0$, but in practice this is relaxed and:

$$\Gamma_\ell = \{\mathbf{x} \in \Omega | d(\mathbf{x}) > \epsilon\} \qquad (34)$$

is taken to define the smeared cohesive crack, with ϵ a small tolerance. According to Equation (33), γ_ℓ can be interpreted as the function that confines the dissipation of energy to the cohesive zone.

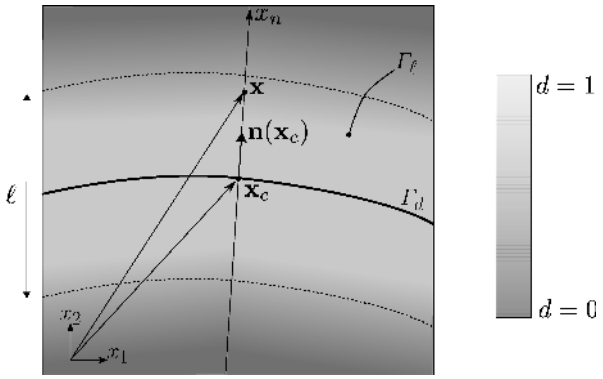

Fig. 10: Γ_d represents the discrete cohesive zone and the centre of the smeared cohesive zone Γ_ℓ

The definition of a discrete quantity like a jump is non-trivial in smeared models. For this purpose an auxiliary field, $\mathbf{v}$, was introduced in Reference [22], and is also used here:

$$\llbracket \mathbf{u} \rrbracket(\mathbf{x_c}) \approx \int_{-\infty}^{\infty} \mathbf{v}(\mathbf{x}) \delta_\ell \mathrm{d}x_n. \qquad (35)$$

The auxiliary field thus approximates the crack opening at any point $\mathbf{x}_c \in \Gamma_d$, i.e. on the discrete crack surface Γ_d. Further, for any point $\mathbf{x} \in \Gamma_\ell$, with Γ_ℓ the area over which the discrete crack has been distributed, it is possible to find the nearest point $\mathbf{x}_c \in \Gamma_d$. Requiring that the auxiliary field $\mathbf{v}$ remains constant in the direction normal to the crack, i.e.

$$\frac{\partial \mathbf{v}}{\partial x_n} = \mathbf{0} \qquad (36)$$

we obtain that

$$\mathbf{v}(\mathbf{x}) = \mathbf{v}\big(\mathbf{x_c} + x_n \mathbf{n}(\mathbf{x}_c)\big) = \mathbf{v}(\mathbf{x_c}) \qquad (37)$$

with $\mathbf{n}$ the normal to the crack, and the displacement jump can be approximated as:

$$\llbracket \mathbf{u} \rrbracket(\mathbf{x_c}) \approx \mathbf{v}(\mathbf{x}_c) \int_{-\infty}^{\infty} \delta_\ell \mathrm{d}x_n = \mathbf{v}(\mathbf{x}_c). \qquad (38)$$

As a consequence of the introduction of the auxiliary field, the fracture energy function becomes

$$\mathcal{G}([\![\mathbf{u}]\!],\kappa) \approx \mathcal{G}(\mathbf{v},\kappa) \tag{39}$$

and the traction in the cohesive zone reads:

$$\mathbf{t}_d(\mathbf{v},\kappa) = \frac{\partial \mathcal{G}(\mathbf{v},\kappa)}{\partial \mathbf{v}} \quad \text{while} \quad \int_0^\infty \mathbf{t}_d(\mathbf{v},\kappa)\mathrm{d}\mathbf{v} = \mathcal{G}_c. \tag{40}$$

The second step of the coupling requires the derivation of the elastic energy density function ψ^e of the damaged model that takes into account crack growth. It relies on the assumption that the total strain $\boldsymbol{\varepsilon}$ can be split into an elastic term and a term that accounts for damage:

$$\boldsymbol{\varepsilon} = \boldsymbol{\varepsilon}^e + \boldsymbol{\varepsilon}^d \tag{41}$$

such that

$$\psi^e(\boldsymbol{\varepsilon},d) = \psi^e(\boldsymbol{\varepsilon}^e) = \psi^e(\boldsymbol{\varepsilon}-\boldsymbol{\varepsilon}^d). \tag{42}$$

This split can be derived explicitly from energy considerations. On one hand, the second principle of thermodynamics gives:

$$\begin{aligned} 0 \leq \dot{\mathcal{D}} &= \sigma_{ij}\dot{\varepsilon}_{ij} - \dot{\psi}_e \\ &= \sigma_{ij}(\dot{\varepsilon}^e_{ij} + \dot{\varepsilon}^d_{ij}) - \frac{\partial \psi_e}{\partial \varepsilon^e_{ij}}\dot{\varepsilon}^e_{ij} \\ &= \sigma_{ij}(\dot{\varepsilon}^e_{ij} + \dot{\varepsilon}^d_{ij}) - \sigma_{ij}\dot{\varepsilon}^e_{ij} \\ &= \sigma_{ij}\dot{\varepsilon}^d_{ij}. \end{aligned} \tag{43}$$

On the other hand, use of Equation (33) allow the explicit evaluation of the energy dissipation rate:

$$\dot{\mathcal{D}} = \frac{\mathrm{d}}{\mathrm{d}t}\Big(\gamma_\ell(d)\mathcal{G}(\mathbf{v})\Big) = \gamma_\ell \mathbf{t}_d \dot{\mathbf{v}} + \mathcal{G}\frac{\partial \gamma_\ell}{\partial d}\dot{d} \tag{44}$$

where $\dot{\mathbf{v}}$ could have equally been replaced by $[\![\dot{\mathbf{u}}]\!]$. The first term in Equation (44) measures the increment of energy dissipated as a result of further opening the existing crack by an increment $\dot{\mathbf{v}}$. The second term corresponds to the energy dissipated through the extension of the *cohesive zone* by an increment $\dot{d}$. Under the hypothesis that the smeared jump $\mathbf{v}$ is initially zero in the newly created cohesive zone, it can be assumed that advancing the cohesive zone as a result of a change $\dot{d}$ in the phase field, is not accompanied by any dissipation of energy as $\mathcal{G}(0) = 0$. Under this assumption and combining Equations (43) and (44), the part of the total strain $\boldsymbol{\varepsilon}$ that purely results from damage evolution can be evaluated as:

$$\dot{\boldsymbol{\varepsilon}}^d = \gamma_\ell \,\mathrm{sym}(\dot{\mathbf{v}} \otimes \mathbf{n}). \tag{45}$$

Consequently, the elastic strain reads:

$$\boldsymbol{\varepsilon}^e = \nabla^s \mathbf{u} - \gamma_\ell \,\mathrm{sym}(\mathbf{v} \otimes \mathbf{n}), \tag{46}$$

with ∇^s the symmetrised gradient operator. If the displacement, the auxiliary and the phase fields are all approximated by piecewise linear functions, the first term in Equation (46) is constant in the one-dimensional case, while the second term is a quadratic polynomial. It was reported in [22] that this order mismatch leads to stress oscillations, and it was suggested that the auxiliary and the phase fields are approximated with linear functions, while the displacements are approximated using cubic polynomials.

Finally, the smeared form of the total potential energy for cohesive fracture becomes

$$\Psi = \int_\Omega \left(\psi^e(\boldsymbol{\varepsilon}^e) + \gamma_\ell\,\mathcal{G}(\mathbf{v}) + \frac{\alpha}{2}\left|\frac{\partial \mathbf{v}}{\partial x_n}\right|^2\right)\mathrm{d}V \tag{47}$$

where a penalty term has been added to enforce the auxiliary field $\mathbf{v}$ to remain constant along the normal of the crack.

4.1.1 Discretised fields

With the potentials of the phase field, Equation (10), and the mechanical field, Equation (47), at hand, we solve them in a staggered manner, similar to [22]. The discrete phase field problem is solved first, in order to initialise the topology of the smeared cohesive crack. This solution is used as an input to solve the discrete mechanical problem. The algorithmic flow is shown in Algorithm 1, while details regarding the mechanical problem are derived below.

The governing equations of the mechanical problem are obtained by minimising the potential, Equation (47):

$$\mathrm{div}\,\boldsymbol{\sigma} = \mathbf{0} \qquad \mathbf{x} \in \Omega \tag{48a}$$

$$\boldsymbol{\sigma}\mathbf{n} = \bar{\mathbf{t}} \qquad \mathbf{x} \in \Gamma \tag{48b}$$

$$\gamma_\ell\big(\mathbf{t}_d - \boldsymbol{\sigma}\mathbf{n}\big) = \alpha\frac{\partial^2 \mathbf{v}}{\partial x_n^2} \qquad \mathbf{x} \in \Gamma_\ell \tag{48c}$$

$$\frac{\partial \mathbf{v}}{\partial x_n} = 0 \qquad \mathbf{x} \in \partial\Gamma_\ell \tag{48d}$$

Note that in the momentum balance, Equation (48a), the Cauchy stress $\boldsymbol{\sigma}$ is a function of the elastic strain only. Furthermore, the crack density function γ_ℓ acts as a switch that enforces the cohesive law in Equation (48c).

As for the brittle model, the weak form is obtained from Equation (48). Approximation of the field variables and their derivatives as

$$\begin{cases}\mathbf{u}(\mathbf{x}) = \mathbf{N}_u(\mathbf{x})\mathbf{u}^e \\ \mathbf{v}(\mathbf{x}) = \mathbf{N}_v(\mathbf{x})\mathbf{v}^e\end{cases} \qquad \begin{cases}\boldsymbol{\varepsilon}(\mathbf{x}) = \mathbf{B}_u(\mathbf{x})\mathbf{u}^e \\ \mathrm{sym}(\mathbf{v}\otimes\mathbf{n}) = \mathbf{B}_v(\mathbf{x})\mathbf{v}^e\end{cases} \tag{49}$$

$$\frac{\partial \mathbf{v}}{\partial x_n} = \mathbf{G}_v(\mathbf{x})\mathbf{v}^e \tag{50}$$

results in a nonlinear set of equations which can be linearised and solved using a Newton-Raphson iterative scheme, again enhanced by the dissipation-based arc-length method [14,21]. The update of the state vector at iteration k can be derived as:

$$\begin{bmatrix}\delta\mathbf{u}\\ \delta\mathbf{v}\\ \delta\lambda\end{bmatrix}_k = \begin{bmatrix}\mathbf{K}_{uu} & \mathbf{K}_{uv} & -\hat{\mathbf{f}}^{\mathrm{ext}}\\ \mathbf{K}_{vu} & \mathbf{K}_{vv} & \mathbf{0}\\ \mathbf{h}^T & \mathbf{0}^T & w\end{bmatrix}^{-1}_{k-1} \begin{bmatrix}\lambda\hat{\mathbf{f}}^{\mathrm{ext}} - \mathbf{f}_u^{\mathrm{int}}\\ -\mathbf{f}_v^{\mathrm{int}}\\ -\psi\end{bmatrix}_{k-1} \tag{51}$$

with:

$$\mathbf{f}_v^{\mathrm{int}} = \int_\Omega -\gamma_\ell \mathbf{B}_v^T\mathbf{C}\mathbf{B}_u\mathbf{u} + \gamma_\ell^2\mathbf{B}_v^T\mathbf{C}\mathbf{B}_v\mathbf{v} + \gamma_\ell\mathbf{N}_v^T\mathbf{t}_d + \alpha\mathbf{G}_v^T\mathbf{G}_v\mathbf{v}\,\mathrm{d}V \tag{52}$$

$$\mathbf{f}_u^{\mathrm{int}} = \int_\Omega \mathbf{B}_u^T\mathbf{C}\mathbf{B}_u\mathbf{u} - \gamma_\ell\mathbf{B}_u^T\mathbf{C}\mathbf{B}_v\mathbf{v}\mathrm{d}V \tag{53}$$

$$\psi = \frac{1}{2}\hat{\mathbf{f}}^{\mathrm{ext}}\left(\lambda_0\Delta\mathbf{u} - \Delta\lambda\mathbf{u}_0\right) - \Delta\tau \tag{54}$$

$$\mathbf{K}_{vv} = \frac{\partial\mathbf{f}_v^{\mathrm{int}}}{\partial\mathbf{v}} \quad \mathbf{K}_{vu} = \frac{\partial\mathbf{f}_v^{\mathrm{int}}}{\partial\mathbf{u}} \tag{55}$$

$$\mathbf{K}_{uv} = \frac{\partial\mathbf{f}_u^{\mathrm{int}}}{\partial\mathbf{v}} \quad \mathbf{K}_{uu} = \frac{\partial\mathbf{f}_u^{\mathrm{int}}}{\partial\mathbf{u}} \tag{56}$$

$$\mathbf{h} = \frac{\partial\psi}{\partial\mathbf{u}} \quad w = \frac{\partial\psi}{\partial\lambda}. \tag{57}$$

4.2 Crack propagation

In Reference [22], the position and growth of the phase field was controlled by a driving force term

$$\mathcal{F} = C\frac{8\ell^2}{h^2}\delta_d(x_n) \tag{58}$$

which results from the addition of a penalty term onto the weak form of the phase field problem, with C the penalty weight and $\delta_d(x_n)$ is the Dirac function centred at Γ_d. A *crack set* $\mathcal{S}$ was then defined, which is a list of Gauss points where $d = 1$. This approach has some disadvantages, since it not only requires an additional parameter and more computations in order to evaluate the driving force, but linear shape functions that enforce $d = 1$ at a Gauss point can lead to nodal phase field variables that locally exceed 1.

Here, we propose to build the centre of the cohesive zone Γ_d with a crack set $\mathcal{S}$ which only contains nodes. Consequently, the driving force $\mathcal{F}$ is no longer required. Upon minimisation of the potential of the phase-field potential, Equation (10), the strong form

$$\begin{cases} d - 4\ell^2\nabla^2 d = 0 & \mathbf{x}\in\Omega \\ d(\mathbf{x}) = 1 & \mathbf{x}\in\Gamma_d \\ \nabla d\cdot\mathbf{n} = 0 & \mathbf{x}\in\Gamma\end{cases} \tag{59}$$

is obtained. Equation (59) implies that the centre of the cohesive zone Γ_d is built using Dirichlet boundary conditions.

Next, the weak form of Equation (59) can be derived and can be discretised via:

$$\begin{cases} d(\mathbf{x}) = \mathbf{N}_d(\mathbf{x})\mathbf{d}^e \\ \dfrac{\partial d(\mathbf{x})}{\partial\mathbf{x}} = \mathbf{B}_d(\mathbf{x})\mathbf{d}^e.\end{cases} \tag{60}$$

The linear phase field problem is then solved for the Dirichlet conditions $\bar{\mathbf{d}} = [1\ldots1]^{\mathrm{T}}$ prescribed at the nodes in the crack set $\mathcal{S}$:

$$\left[\mathbf{K}_{dd}\right]\begin{bmatrix}\mathbf{d}^e\\ \bar{\mathbf{d}}\end{bmatrix} = \mathbf{f}_d^{\mathrm{ext}} = \mathbf{0} \tag{61}$$

with

$$\mathbf{K}_{dd} = \int_\Omega \mathcal{G}_c\frac{1}{2\ell}\mathbf{N}_d^T\mathbf{N}_d + 2\ell\mathbf{B}_d^T\mathbf{B}_d\,\mathrm{d}V. \tag{62}$$

Finally, the crack density is evaluated according to:

$$\gamma_\ell = \mathbf{d}^{\mathrm{T}}\Big(\frac{1}{4\ell}\mathbf{N}_d^{\mathrm{T}}\mathbf{N}_d + \ell\mathbf{B}_d^{\mathrm{T}}\mathbf{B}_d\Big)\mathbf{d}. \tag{63}$$

At the beginning of the simulation, the crack set $\mathcal{S}^0$ is an inventory of nodes locating a potential initial defect. For the first iteration ($j = 0$) of any subsequent increment i, the crack set is initially frozen to the previously converged state: $\mathcal{S}^i_{j=0} = \mathcal{S}^{i-1}_{\mathrm{final}}$. The mechanical field problem is solved iteratively until a balance has been obtained between the internal and the external loads. The nucleation criterion is then evaluated with the updated displacement and jump fields $\{\mathbf{u}^e, \mathbf{v}^e\}^i_{j=0}$. As in [22], the maximum principal stress is used as the propagation criterion. This has the additional benefit of directly providing the crack normal vector.

When the major principal stress σ^1 exceeds the fracture strength t_u, the crack must be advanced to dissipate more energy. The Gauss point $\mathrm{GP}_j = \max_{\mathbf{x}\in\mathrm{GP}}\left(\sigma_j^1(\mathbf{x})\right)$ is identified, and the node N_j closest to GP_j is added to the crack set, which becomes $\mathcal{S}^i_{j=1}$. Confining the crack set to nodes can result in a mesh

dependence. This is circumvented by shifting the node N_j to the location of GP_j. The phase-field problem is then solved and the crack density is updated. The mechanical field problem must be updated for the same increment i with the new crack set $\mathcal{S}^i_{j=1}$.

Once equilibrium has been obtained, the nucleation criterion is checked again. If it is not violated, one can advance to the next increment. Otherwise a new phase-field distribution must be obtained. The procedure is repeated until the loads are in equilibrium and the nucleation criteria is violated nowhere.

4.3 Example 1: Propagating crack along a predefined path

The delamination peel test of [22] is revisited with the developments presented in the previous section. The geometry of the beam is depicted in Figure 11 and the elastic parameters are $E = 100$MPa and $\nu = 0.3$. The fracture strength and energy are taken as $t_u = 1$MPa and $\mathcal{G}_c = 0.1$N/mm.

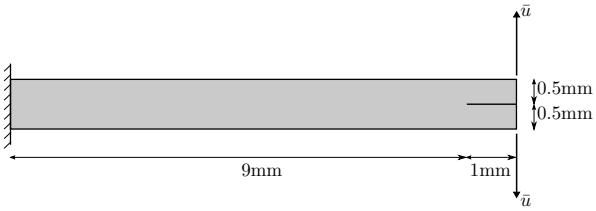

Fig. 11: Geometry of the propagating crack example

The decohesion relation is chosen as

$$t_d(v) = \begin{cases} t_u + kv & v \leq 0 \\ t_u \exp\left(-\frac{t_u}{\mathcal{G}_c} v\right) & v > 0 \end{cases} \tag{64}$$

where k prevents crack interpenetration. Herein, $k = 1 \cdot 10^4$MPa/mm has been used. The tolerance ϵ, that defines the cohesive zone, Equation (34), is taken as $1 \cdot 10^{-2}$. The penalty parameter that enforces the constant jump in the direction normal to the crack is taken as $\alpha = t_u$.

The purpose of this test is to demonstrate the ability of the current formulation to model a propagating crack along a predefined path. Hence, instead of allowing the crack to curve away from the centre line of the beam, it is forced to remain straight and to grow along the centre line. Consequently, the crack normals are predefined and set such that $\mathbf{n} = \{0, 1\}$.

In the following, we consider:

- two mesh sizes: a coarse mesh with $h = 0.1$mm and a finer mesh with $h = 0.05$mm. For both meshes, the length scale is taken as $\ell = 0.1$mm.
- two mesh types: *structured* and *unstructured*, Figures 12a and 12d, respectively. The unstructured meshes are generated by a routine that shifts the nodes of the structured mesh by a random amount in the interval $[-0.1h; 0.1h]$. To further perturb the structure of the mesh, this routine can be run successively n times, which will be referred to as 'n-loops'.
- two schemes: in the *constant mesh* case, the nodal coordinates are frozen for the entire simulation. For the *moving mesh*, the moving node algorithm described in Section 4.2 is used.

In order to allow for a fair comparison between the various cases, we consistently enforce nodes in the crackset to be located on the centre line of the beam. This means that for the moving mesh scheme, the moving nodes can only align laterally with the x-coordinate offending Gauss point. For the structured mesh, nodes cannot move vertically, see Figure 12c. For the unstructured mesh, nodes are forced to move to the centre line of the beam, Figure 12d.

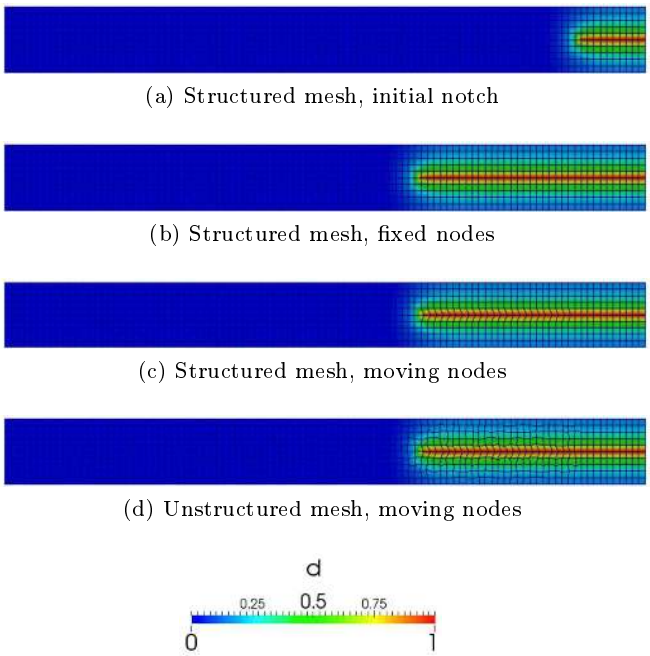

(a) Structured mesh, initial notch

(b) Structured mesh, fixed nodes

(c) Structured mesh, moving nodes

(d) Unstructured mesh, moving nodes

Fig. 12: Phase field distribution: at the beginning of the simulation (a), and for $\bar{u} = 1.5$mm (b)–(d). 100×10 elements ($h \approx 0.1$mm).

It is observed from Figure 13 that for a given external load, the model evaluates the same cohesive zone

for a structured mesh with fixed nodes, as well as for a structured and an unstructured mesh with moving nodes. The force-displacement response of the model for the various cases is shown in Figure 13. We first note that for sake of clarity, the results for the structured fine mesh – with constant and with moving nodes – are not presented as they are very close to those of the coarse mesh. This confirms that the shown results represent the converged solution. Figure 13 also shows that the model is able to predict the critical load and the first part of the softening regime for unstructured meshes, even if thereafter the curves diverge progressively. This phenomenon is more marked when the structure of the mesh is perturbed more strongly.

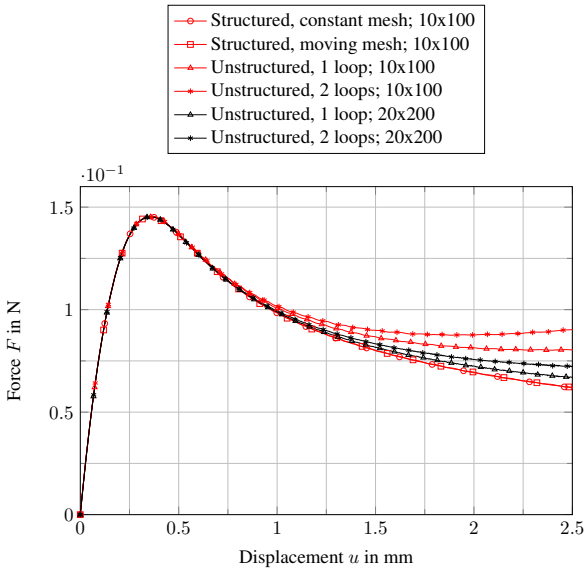

Fig. 13: Force-displacement relation for various meshes and different numbers of perturbation loops

The slow departure from the converged solution for the structured meshes can be explained by considering the elastic strain distribution ε^e_{yy} in the cohesive zone. As shown in Figure 14a for $\bar{u} = 0.75$mm, a wavy pattern in the elastic strain evolves in the wake of the crack tip, see also Figure 14b. These patterns are not observed for the structured mesh. These strain oscillations tend to lock the elastic strains, and therefore the stresses in the cohesive zone, which causes the stiffer response observed in Figure 13. This phenomenon can have several causes. The elementary method used to generate unstructured meshes resulted in a relatively poor mesh quality. The use of cubic Lagrange functions for the displacements can be another reason. Potential solutions are to use mesh improvement technologies, stress smoothing, or the use of splines (isogeometric analysis).

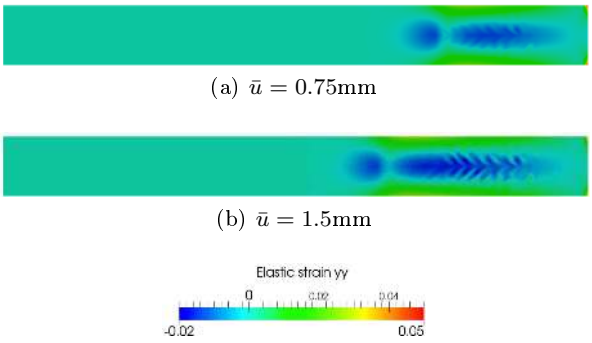

(a) $\bar{u} = 0.75$mm

(b) $\bar{u} = 1.5$mm

Fig. 14: Contour plot of the elastic strain ε^e_{yy} for the unstructured 100×10 mesh after two perturbation loops

4.4 Example 2: Bar with reduced stiffness

The 1D bar problem of Section 3.3 is revisited, now using the cohesive model, but with the same dimensions and elastic properties. A strictly decaying traction relation is used:

$$t_d = t_u \exp\left(-\frac{t_u}{\mathcal{G}_c}[\![u]\!]\right) \approx t_u \exp\left(-\frac{t_u}{\mathcal{G}_c} v\right) \tag{65}$$

with the fracture strength $t_u = 2$MPa. Following [22] the penalty parameter that enforces the constant jump in the direction normal to the crack is chosen as $\alpha = t_u$. Force control is applied up to the peak load, where the solver switches to the dissipative arc-length method. In theory, all Gauss points in the area with reduced stiffness reach the fracture strength in the same increment. However, as fracture is expected to occur locally, only a single node is added to the crack set. As described before, the mesh is modified by shifting the node closest to this Gauss point.

First, the influence of the mesh size is investigated. Figure 15 shows that in the snapback regime, convergence is obtained with much less elements than with the brittle fracture model for $\ell = 0.05$mm.

Next, the impact of the length scale parameter ℓ is assessed. From Figure 16 we observe that the length scale parameter ℓ has no influence on the linear elastic regime, and neither on the peak load. A limited influence is observed in the post-peak regime. This means that, at variance with the brittle case, the influence of ℓ is strictly confined to the topological approximation and does not govern the overall mechanical behaviour of the structure. It is also noted that the response is perfectly linear up to the maximum load.

Finally, we have investigated the approximated crack length Γ_ℓ at failure, evaluated using quation (12). The exact crack length is $\Gamma_d = h/2 = 0.5$mm and the relative error is given by Equation (32). Figure 17 shows, for three different length scales, that the crack

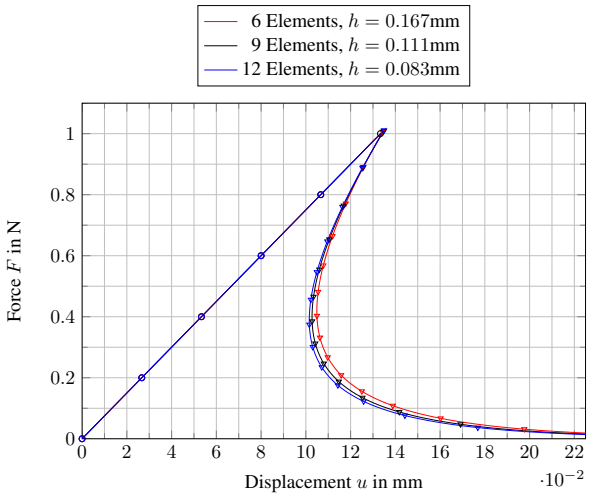

Fig. 15: Mesh refinement for constant length scale parameter $\ell = 0.05$mm

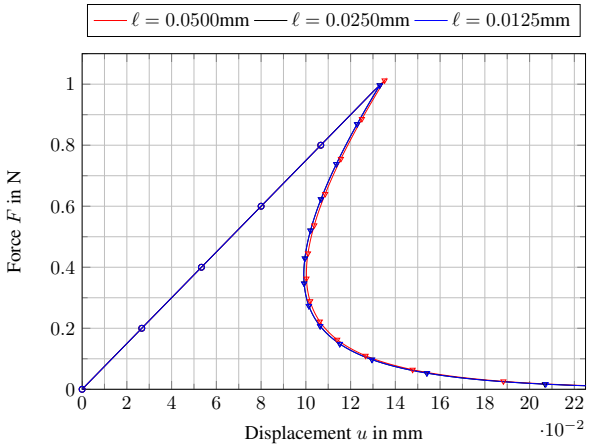

Fig. 16: Influence of length scale parameter ℓ for constant number of 300 elements. The results for $\ell = 0.025$mm and $\ell = 0.0125$mm almost coincide.

length approximation converges upon mesh refinement (although denser meshes would be required for $\ell = 0.0125$mm), but also that the quality of the approximation increases as the length scale decreases. A convergence study in Reference [19] indicates that, for the phase field problem only, this observation is only valid for the discretised problem when the length scale is larger than the mesh size, which seems to be in agreement with the current results.

5 Concluding remarks

The present investigation confirms that phase field models give qualitatively good results for brittle fracture, both for mode-I and for mode-II problems [18, 19]. However, the model can be sensitive. Using a simple one-dimensional bar with a defect in the centre part, it was shown that the choice of the degradation function may considerably influence the results, as does the choice of the length scale parameter ℓ. The latter observation makes it difficult to interpret the length scale parameter for the brittle phase field model. Its introduction on mathematical grounds would point to a parameter for the phase field that does not influence the mechanical field problem, but this is not confirmed in actual computations in which the phase field and the mechanical field are lined [1,4]. Another finding is that solving the phase field and the mechanical field using a monolithic scheme leads to a faster convergence with respect to mesh refinement, compared to a partitioned solution strategy.

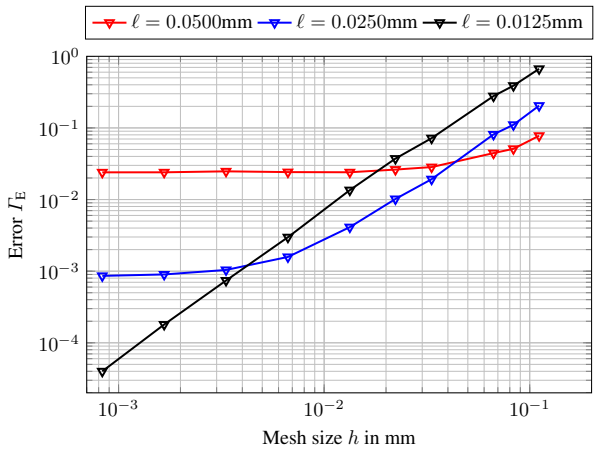

Fig. 17: Error Γ_{E} for the final crack length Γ_ℓ

In the last part of the paper the cohesive phase field approach [22] is revisited and further elaborated, in particular for propagative cohesive cracks. From the theoretical side, a new, thermodynamically motivated way to decompose the strain field into an elastic contribution and a smeared crack contribution has been proposed. From the implementation side, a crack set has been suggested that only contains nodes, rather than integration points. To obviate loss of flexibility and ameliorate possible crack bias, nodes are allowed to move towards integration points were the fracture criterion has been violated (r-adaptivity). An advantage is that a driving force term [22] is not needed, thereby reducing the number of numerical parameters. Example calculations – with structured and unstructured meshes, and with fixed and moving nodes – on adhesive crack propagation in a cantilever beam show the potential of the method, although the extension to arbitary crack propagation remains a challenge. Finally, revisiting the one-dimensional example used in the beginning for brit-

tle crack propagation shows that far less elements are now needed to achieve convergence, and, more importantly, that the results are now virtually insensitive to the value of the length scale parameter ℓ.

References

1. Amor, H., Marigo, J.J., Maurini, C.: Regularized formulation of the variational brittle fracture with unilateral contact: Numerical experiments. Journal of the Mechanics and Physics of Solids **57**(8), 1209–1229 (2009)
2. Barenblatt, G.: The mathematical theory of equilibrium cracks in brittle fracture. Academic Press Inc. (1962)
3. Borden, M.: Isogeometric analysis of phase-field models for dynamic brittle and ductile fracture. Ph.D. thesis, The University of Texas at Austin (2012)
4. Borden, M., Verhoosel, C., Scott, M., Hughes, T., Landis, C.: A phase-field description of dynamic brittle fracture. Computer Methods in Applied Mechanics and Engineering **217-220**, 77–95 (2012)
5. de Borst, R., Mühlhaus, H.B., Pamin, J., Sluys, L.J.: Fundamental issues in finite element analyses of localization of deformation. Engineering Computations **10**, 99–121 (1993)
6. Bourdin, B., Francfort, G., Marigo, J.J.: Numerical experiments in revisited brittle fracture. Journal of the Mechanics and Physics of Solids **48**(4), 797 – 826 (2000)
7. Bourdin, B., Francfort, G., Marigo, J.J.: The variational approach to fracture. Journal of Elasticity **91**(1-3), 5–148 (2008)
8. Bourdin, B., Larsen, C.J., Richardson, C.: A time-discrete model for dynamic fracture based on crack regularization. International Journal of Fracture **168**, 133–143 (2011)
9. Camacho, G.T., Ortiz, M.: Computational modelling of impact damage in brittle materials. International Journal of Solids and Structures **33**, 2899–2938 (1996)
10. Chambolle, A.: An approximation result for special functions with bounded deformation. Journal de Mathématiques Pures et Appliquées **83**(7), 929 – 954 (2004)
11. Dugdale, D.: Yielding of steel sheets containing slits. Journal of the Mechanics and Physics of Solids **8**(2), 100–104 (1960)
12. Francfort, G., Marigo, J.J.: Revisiting brittle fracture as an energy minimization problem. Journal of the Mechanics and Physics of Solids **46**(8), 1319–1342 (1998)
13. Freddi, F., Royer-Carfagni, G.: Regularized variational theories of fracture: A unified approach. Journal of the Mechanics and Physics of Solids **58**(8), 1154–1174 (2010)
14. Gutiérrez, M.A.: Energy release control for numerical simulations of failure in quasi-brittle solids. Communications in Numerical Methods in Engineering **20**(1), 19–29 (2004)
15. Hofacker, M., Miehe, C.: Continuum phase field modeling of dynamic fracture: variational principles and staggered fe implementations. International Journal of Fracture **178**, 113–129 (2012)
16. Ingraffea, A.R., Saouma, V.: Numerical modelling of discrete crack propagation in reinforced and plain concrete. In: Fracture Mechanics of Concrete, pp. 171–225. Martinus Nijhoff Publishers, Dordrecht (1985)
17. Lancioni, G., Royer-Carfagni, G.: The variational approach to fracture mechanics. a practical application to the French Pantheon in Paris. Journal of Elasticity **95**, 1–30 (2009)
18. Miehe, C., Hofacker, M., Welschinger, F.: A phase field model for rate-independent crack propagation: Robust algorithmic implementation based on operator splits. Computer Methods in Applied Mechanics and Engineering **199**(45-48), 2765 – 2778 (2010)
19. Miehe, C., Welschinger, F., Hofacker, M.: Thermodynamically consistent phase-field models of fracture: Variational principles and multi-field fe implementations. International Journal for Numerical Methods in Engineering **83**(10), 1273–1311 (2010)
20. Peerlings, R.H.J., de Borst, R., Brekelmans, W.A.M., de Vree, H.P.J.: Gradient-enhanced damage for quasi-brittle materials. International Journal for Numerical Methods in Engineering **39**, 3391–3403 (1996)
21. Verhoosel, C., Remmers, J.J.C., Gutierrez, M.: A dissipation-based arc-length method for robust simulation of brittle and ductile failure. International Journal for Numerical Methods in Engineering **77**(9), 1290–1321 (2009)
22. Verhoosel, C.V., de Borst, R.: A phase-field model for cohesive fracture. International Journal for Numerical Methods in Engineering **96**, 43–62 (2013)

For *Increment* i **do**
- **Initialise**
  - The external loading: either $\bar{\mathbf{u}}$, $\bar{\lambda}$ or $\Delta\tau$;
  - The initial crack set: $\mathcal{S}_{j=0}^{i} = \mathcal{S}_{\text{final}}^{i-1}$;
  - The internal force vectors $\mathbf{f}_v^{\text{int}}$ and $\mathbf{f}_u^{\text{int}}$;
  - The residual: $\mathbf{R}_0 = [\mathbf{f}_v^{\text{ext}}\ \mathbf{f}_u^{\text{ext}}]^{\text{T}} - \left[\mathbf{f}_v^{\text{int}}\ \mathbf{f}_u^{\text{int}}\right]^{\text{T}}$;

- **Do** *Crackset loop* j **while** $\mathcal{S}_{j+1} \not\subset \mathcal{S}_j$
  - **Do** *Iterative Newton loop* k *for the mechanical field problem* **while** $||R|| > \varepsilon$
    - CRACK OPENING ;
    - **Evaluate**
      - The global stiffness matrices $\mathbf{K}_{vv}$, $\mathbf{K}_{vu}$, $\mathbf{K}_{uv}$, $\mathbf{K}_{uu}$;
      - The incremental state vector $[\delta\mathbf{v}\ \delta\mathbf{u}]_k^{\text{T}}$;
    - **Update**
      - The state vector $[\mathbf{v}\ \mathbf{u}]_k^{\text{T}}$;
      - The internal force vectors $\mathbf{f}_v^{\text{int}}$ and $\mathbf{f}_u^{\text{int}}$;
      - The residual $\mathbf{R}_k = [\mathbf{f}_v^{\text{ext}}\ \mathbf{f}_u^{\text{ext}}]_k^{\text{T}} - \left[\mathbf{f}_v^{\text{int}}\ \mathbf{f}_u^{\text{int}}\right]_k^{\text{T}}$;
  - **end**
  - **if** $\boldsymbol{\sigma}_j^1 > t_u$ **then**
    - EXTENSION OF THE COHESIVE ZONE ;
    - **Evaluate**
      - Principal stresses σ_j^1 and σ_j^2 ;
      - Principal directions $\mathbf{n}^1$ and $\mathbf{n}^2$;
    - **Locate**
      - The Gauss point $\text{GP}_j = \max_{\mathbf{x}\in\text{GP}} \left(\sigma_j^1(\mathbf{x})\right)$;
      - The closest node N_j to GP_j
    - **Update**
      - The mesh: move N_j to the location of GP_j;
      - The crack set $\mathcal{S}_j$ with N_j ;
    - **Solve**
      - The phase field problem with the new boundary conditions ;
    - **Update**
      - The crack density functional γ_ℓ ;
      - The normal at Gauss points in the cohesive zone Γ_ℓ ;
  - **end**
- **end**

end

Algorithm 1: Algorithm for the cohesive model